





High-entropy engineering with regulated defect structure and electron interaction tuning active sites for trifunctional electrocatalysis

Xiaoxiao Zou^a, Jiyang Xie^a, Zhiyuan Mei^a, Qi Jing^a, Xuelin Sheng^a, Conghui Zhang^a, Yongxin Yang^a, Mengjiao Sun^a, Futong Ren^a, Lilian Wang^a, Tianwei He^{a,1} , Youchao Kong^{b,1}, and Hong Guo^{a,c,1} 

Edited by Alexis Bell, University of California, Berkeley, CA; received August 8, 2023; accepted January 30, 2024

High-entropy alloy nanoparticles (HEANs) possessing regulated defect structure and electron interaction exhibit a guideline for constructing multifunctional catalysts. However, the microstructure–activity relationship between active sites of HEANs for multifunctional electrocatalysts is rarely reported. In this work, HEANs distributed on multi-walled carbon nanotubes (HEAN/CNT) are prepared by Joule heating as an example to explain the mechanism of trifunctional electrocatalysis for oxygen reduction, oxygen evolution, and hydrogen evolution reaction. HEAN/CNT excels with unmatched stability, maintaining a 0.8V voltage window for 220 h in zinc–air batteries. Even after 20 h of water electrolysis, its performance remains undiminished, highlighting exceptional endurance and reliability. Moreover, the intrinsic characteristics of the defect structure and electron interaction for HEAN/CNT are investigated in detail. The electrocatalytic mechanism of trifunctional electrocatalysis of HEAN/CNT under different conditions is identified by in situ monitoring and theoretical calculation. Meanwhile, the electron interaction and adaptive regulation of active sites in the trifunctional electrocatalysis of HEANs were further verified by density functional theory. These findings could provide unique ideas for designing inexpensive multifunctional high-entropy electrocatalysts.

high-entropy alloy nanoparticles | trifunctional electrocatalysis | defect structure | electron interaction

With the increasing popularity of renewable electricity, electrocatalytic conversion has become one of the most promising ways to achieve energy conversion and green chemical synthesis. However, how to optimize the structure of the catalyst and establish its structure–activity relationship with the catalytic process is still a huge challenge (1–4). HEANs (high-entropy alloy nanoparticles) have received a lot of attention because of their multi-element composition, homogeneously mixed solid solution state, and large specific surface area. Because each element has different atomic radii, chemical bonding, and crystal structure, mixing so many elements increases lattice distortion, so the flexibility for crystallographic defect optimizes the electronic structure of HEANs allowing catalytic activity and selectivity to be fine-tuned (5–9). Meanwhile, the multi-element synergy in HEANs provides different adsorption sites, making them ideal for multi-step tandem or multifunctional catalyst reactions and reducing the number of precious metals (10). Nevertheless, the wide range of possible compositions, complex atomic arrangements, and the research on the surface, order, defect, and dynamic evolution through accurate structural characterization, as well as the identification and understanding of the active sites and performance sources, have seriously limited the development of HEANs (11, 12).

Recently, in the progress of ultrafast synthesis methods, the instantaneous high temperature using Joule heating makes the mixed metal salt pyrolyze and form metal droplets at the same time (13–15). Compared with the traditional external source heating method, internal source heating has the characteristics of less energy consumption, high energy utilization, fast rising/cooling rate, and uniform product division (16). Based on the method of non-equilibrium carbon-thermal shock, a variety of phase-free high-entropy materials (HEMs) have been synthesized. High-entropy oxide nanoparticles dispersion on commercial carbon black synthesized by Joule heating showed better performance in electrocatalytic oxygen reduction reaction (ORR) (17). Moreover, electrocatalytic reaction is a key part of energy conversion and storage, and the versatility of materials needs to be integrated into equipment for their application. However, HEANs have been found to have excellent multifunctional catalytic performance, and it is still challenging to identify the catalytic active source due to their complex microstructure and binding energy distribution patterns (18). In addition to the diversity of active sites, the effect of crystal defects on the catalytic activity and the adaptive regulation of active sites for HEANs is

Significance

High-entropy materials (HEMs) are considered one of the most promising multifunctional electrocatalysts due to their tunable composition, electronic structure, and excellent stability. However, a limited understanding of the relationship between metal sites and reaction intermediates in HEMs hinders their development in catalysis. Therefore, the need for the identification of active sites is increasing rapidly in the highly complex and diverse class of catalysts with HEMs. Studies to determine the chemical properties of different adsorbed intermediate species on HEMs are critical to understanding multifunctional electrocatalytic reactions. This work reports a trifunctional high-entropy alloy nano-electrocatalyst and provides unique ideas for the design of high-entropy alloy nanoparticles as multifunctional catalysts.

Author contributions: X.Z. and H.G. designed research; X.Z., Q.J., and X.S. performed research; X.Z., J.X., Z.M., C.Z., Y.Y., M.S., F.R., T.H., and Y.K. contributed new reagents/analytic tools; X.Z. and L.W. analyzed data; Y.Y., M.S., and F.R. conducted X-ray diffraction measurements; T.H. and Y.K. conducted theoretical calculations; and X.Z. wrote the paper.

The authors declare no competing interest.

This article is a PNAS Direct Submission.

Copyright © 2024 the Author(s). Published by PNAS. This article is distributed under [Creative Commons Attribution-NonCommercial-NoDerivatives License 4.0 \(CC BY-NC-ND\)](https://creativecommons.org/licenses/by-nc-nd/4.0/).

¹To whom correspondence may be addressed. Email: he.tianwei@ynu.edu.cn, yb87816@um.edu.mo, or guohong@ynu.edu.cn.

This article contains supporting information online at <https://www.pnas.org/lookup/suppl/doi:10.1073/pnas.2313239121/-/DCSupplemental>.

Published March 18, 2024.

rarely reported. Furthermore, the versatility of HEANs has been continuously predicted by theoretical calculations, but few articles have reported the trifunctional catalytic effect (19–22).

Hence, in this work, HEANs are distributed on multi-walled carbon nanotubes (HEAN/CNT) synthesized by Joule heating as an example to explain the mechanism of trifunctional electrocatalysis depicted in Fig. 1. Particularly, we further identify 1) the defect structure, 2) the electron interaction, and 3) the adaptive regulation of active sites in trifunctional electrocatalysis in HEAN/CNT. High entropy leads to defect structure, and both high entropy and defect structure lead to the change of electronic configuration. Both can accelerate the rate of reactant adsorption, accelerate the reactant diffusion on the catalyst surface, and promote the rapid transfer of electrons. Meanwhile, the prepared HEAN/CNT has the versatility of ORR, oxygen evolution reaction (OER), and hydrogen evolution reaction (HER) and shows good stability in zinc–air batteries and electrolytic water. The good trifunctionality results from the lattice defect structure and the electron interaction among the elements of HEANs. Based on the nano-scale surface enhancement effect of the material, the apparent peak intensity variation was detected by the direct in situ Raman. It can be proved that the multi-walled carbon nanotubes (MWCNTs) can be changed from semiconductor properties to metallicity at different potentials, and the loaded HEANs can expose varied active sites suitable for diverse catalytic reaction processes. The synergistic effect between MWCNTs and HEANs gives the material excellent stability in catalysis. In situ Fourier transform infrared (FTIR) further confirmed the mechanism of different reaction processes. Moreover, the theoretical results also verified the electron interaction and the adaptive regulation of active sites for excellent properties of the trifunctional catalysis on HEANs.

Results and Discussion

Materials Characterization. The distribution of HEANs onto MWCNTs can be seen from the dark field image in the scanning transmission electron microscope (STEM) of Fig. 2A. The presence of strain is usually observed when two or more atoms with different radii are mixed. The strain effect can change the electronic structure and geometric structure of the material, thus adjusting the adsorption energy to affect the electrochemical

reaction activity. So, to characterize the morphology and structure of HEANs more accurately, aberration-corrected high-angle annular dark-field STEM (AC-HAADF-STEM) was used. Fig. 2B shows the presence of small black dots (indicated by arrows) and dislocation structures (indicated by lines) in the lattice. The precursor forms a large number of nuclei as a result of rapid heating, and the thermodynamic versus kinetic reaction control causes unconventional grain growth through particle collisions and coalescence, as a result, many vacancies, dislocations, and point defects occur in the nanocrystalline of HEAN/CNT. In addition, defects can be reflected by geometrical phase analyses (GPA) techniques which is a widely used method for strain quantification (23, 24). Under lattice distortion, both shear strain (ϵ_{xy}) and axial strain (ϵ_{xx}) (which can be a compressive strain or tensile strain) appear in HEAN/CNT. Fig. 2C further quantitatively analyses the distribution of strains along the HEANs, which shows more intuitively the distribution of stress and strain caused by the existence of various defective structures. GPA analysis shows that both axial strain and shear strain are distributed in HEANs, and their maximum values are $\epsilon_{xx} = 5\%$ and $\epsilon_{xy} = 5\%$, respectively, indicating that the shear strain and axial strain are the main causes of lattice distortion. Defects introduce additional interfaces and surfaces into the crystal structure, increasing the active area of the material. In addition, we further confirmed the interaction between the interface of HEANs and MWCNTs with AC-HAADF-STEM. As shown in *SI Appendix, Fig. S1*, a severely distorted structure of HEANs and the amorphous structure of MWCNTs in the interface was observed, which indicated the strong binding between HEANs and MWCNTs (25).

Furthermore, the diffraction patterns in the fast Fourier transform (FFT) in Fig. 2D showed face center cubic structures and found distinct diffraction fringes (26–28). Simultaneously, the FFT of different positions were shown in *SI Appendix, Fig. S2A*, it can be seen that the FFT of different positions was slightly distorted. However, no diffraction fringes were found in Pt/CNT (*SI Appendix, Fig. S2 E and F*). These results further demonstrate the defect structure of the HEANs lattices in HEAN/CNT. The three lines drawn from Fig. 2E also demonstrate the existence of surface vacancies shown in Fig. 2F (29, 30). Meanwhile, the single-phase structure of the material was illustrated by the powder X-ray diffraction (XRD) (*SI Appendix, Fig. S3A*), the wide and low diffraction peak in XRD indicate that the HEAN/CNT has the characteristics of small grain size, low degree of crystallization, and many defects, which corresponds to the FFT. At the same time, the illustration in the diagram shows the temperature curve for the synthesis. The current and voltage conditions used for the synthesis of the HEAN/CNT are shown in *SI Appendix, Fig. S3B*. In addition, the dark-field energy-dispersive spectroscopy (EDS) of HEAN/CNT was measured at different resolutions. The corresponding EDS of Fig. 2E and *SI Appendix, Fig. S4A* show the existence and uniform distribution of various elements. However, in *SI Appendix, Fig. S4B*, IFHEAN/CNT exhibits a distinct pattern of agglomeration and segregation, which corresponds to the XRD in *SI Appendix, Fig. S5A*, with the appearance of other peaks and strong diffraction peaks. From the results of XRD, it can also be seen that compared with the four elements mixed to get the polyphase structure, it is easier to get the single-phase structure in the five elements mixed, which means that the high configuration entropy makes it easier to form single-phase solid solution structure. It also indicates that the internal heat source heating with the current impingement method has a faster heating rate than the external heat source of infrared rapid heating and can better mix different elements evenly. *SI Appendix, Table S1* further verifies the content of Fe, Co, Ni, Cu, and Pt, which matched

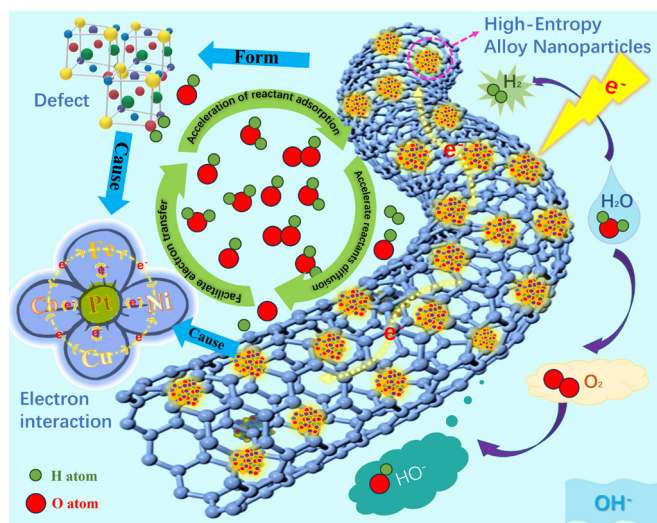


Fig. 1. Schematic illustration of the defect structure and electron interaction for HEAN/CNT in trifunctional electrocatalysis for ORR, OER, and HER.

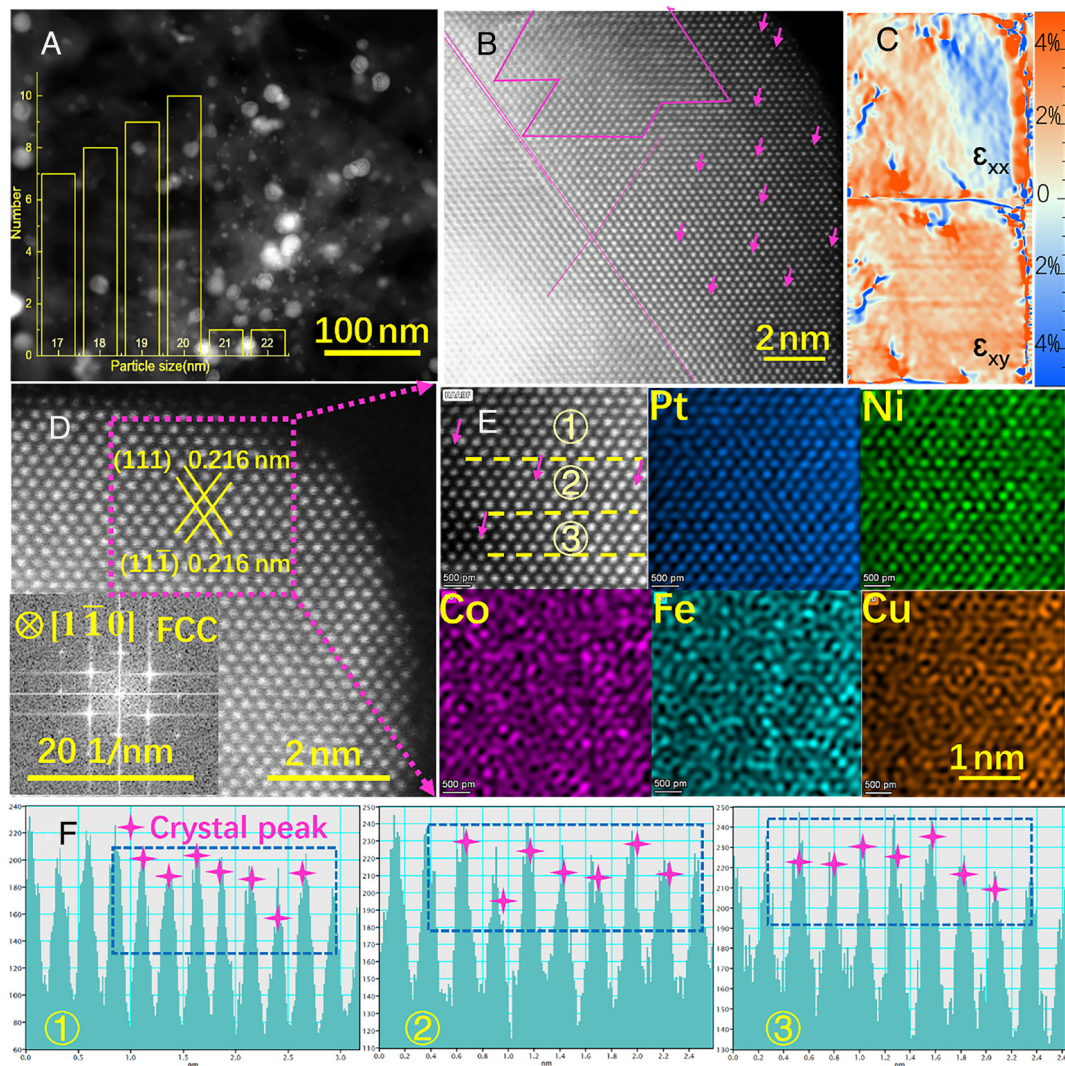


Fig. 2. (A) STEM image of HEAN/CNT (the insert diagram shows the diameter distribution of HEANs), (B) AC-STEM images with multiple crystal defects, (C) the corresponding GPA images for axial strain (ϵ_{xx}) and shear strain (ϵ_{xy}), (D) AC-HRTEM and insert FFT image, and (E) the corresponding atomic-level EDS maps. (F) Line profile of the AC-STEM image of corresponding the three lines ①②③ in (E) of HEANs for HEAN/CNT.

with inductively coupled plasma mass spectroscopy (ICP-MS) in *SI Appendix, Fig. S5B*, where a relatively low Pt content of 5.1466 wt% is identified by ICP-MS in HEAN/CNT.

Electron Interaction. To better understand the electronic effects of HEAN/CNT, electron paramagnetic resonance was carried out. It can be seen from *SI Appendix, Fig. S6* that the electroshock method has more unpaired electrons than the infrared fast-heating furnace, the addition of different elements will affect the electronic arrangement of the material, which confirms HEANs' electron interaction in HEAN/CNT. Moreover, the addition of platinum also significantly changes the spin state of the electron. Electron energy loss spectroscopy (EELS) was used to explore the carbon and oxygen on the surface of the HEANs and the adjacent areas in HEAN/CNT (Fig. 3A). The peaks of carbon and oxygen on the HEANs were the same as those on the MWCNTs indicating that the HEANs exist in the form of alloy, and metal elements cannot react with oxygen under the impact of extremely short electric current (31, 32). Moreover, X-ray absorption fine structure (XAFS) was used to study the electronic structure and coordination environment of HEANs in HEAN/CNT. Fig. 3 B–F are the normalized X-ray absorption near-edge structure (XANES) spectra for Fe K-edge, Co K-edge, Ni K-edge, Cu K-edge, and Pt

L_3 -edge of HEAN/CNT, corresponding foil and metal oxidation, inset with their derivative results. The results show that the valence states of the elements in HEAN/CNT are between their metal state and oxidation state, which further shows that all five elements are in the metallic state and the interaction of the electrons for each element (33, 34). In addition, from the EXAFS fitting results of five elements (*SI Appendix, Fig. S7*), we can see that the coordination number of the first shell is similar, which indicates that the coordination environment of these elements in HEAN/CNT is similar. Meanwhile, it can be seen that Pt is the most difficult to bind to oxygen, while Fe and Ni are the easiest to bind to oxygen and thus contain more oxidized states. X-ray photoelectron spectroscopy (XPS) in *SI Appendix, Fig. S8* has further confirmed the above experimental results.

Compared with single metals, HEANs have lower degeneracy at energy levels, where each atom loses its element identity and can generate an ideal local charge distribution by adjusting adjacent atoms, which is characteristic of HEMs (18). To further understand the interactions among different metals, the density functional theory (DFT) calculations were employed to give some insight from the atomic level. Then, 250 structures of HEANs were built and the most stable model was selected for the whole calculations (Fig. 3G). The details of the construction and selection of HEANs

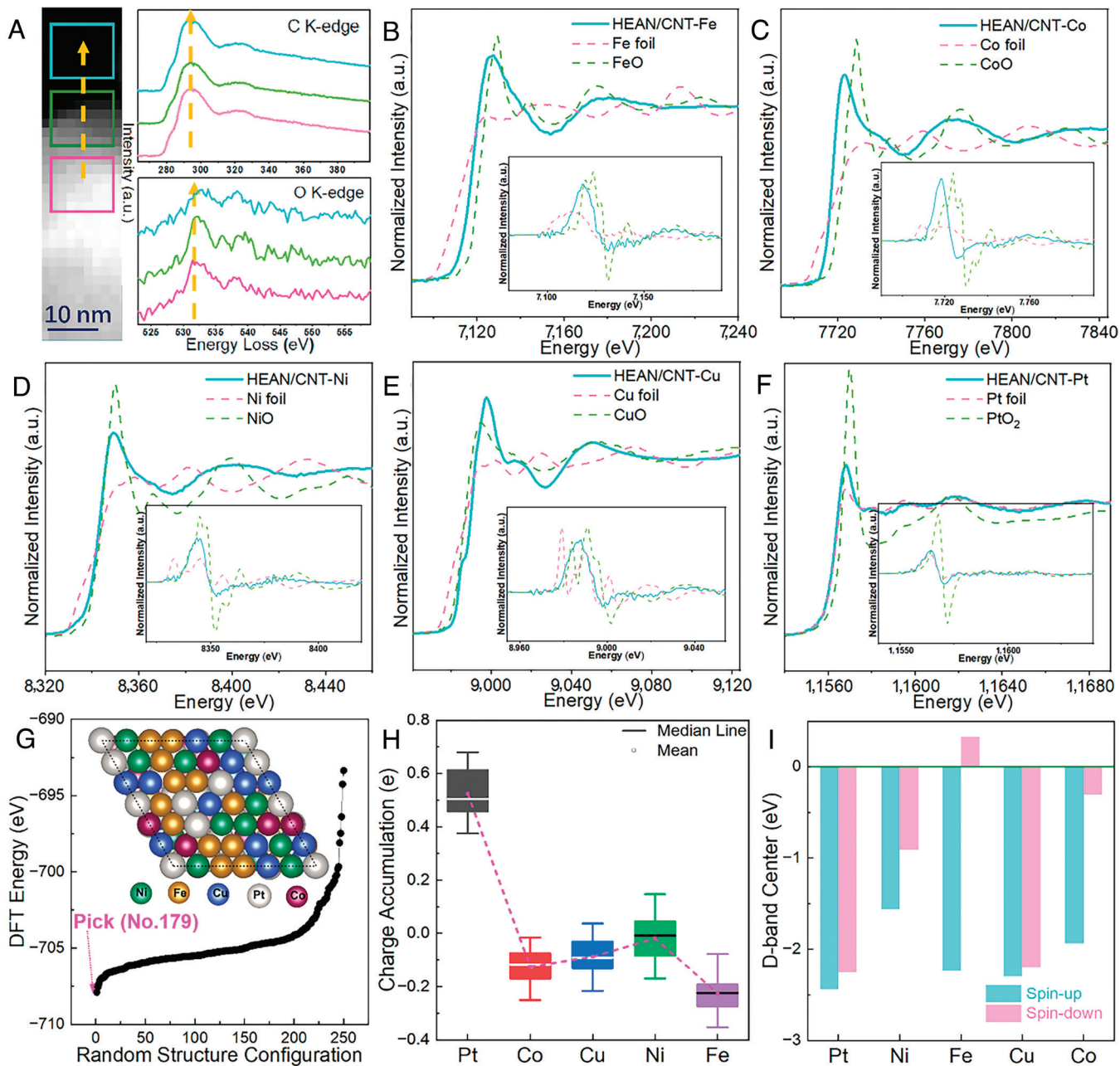


Fig. 3. (A) STEM image and corresponding EELS signals for C and O at various parts, (B–F) Fe K-edge, Co K-edge, Ni K-edge, Cu K-edge, and Pt $L_{2,3}$ -edge XAS spectra and corresponding derivative curves for HEAN/CNT. (G) The formation energy of 250 structures is considered with a stochastic mixing method. (H) Bader charge analysis and (I) the D-band projected DOS (PDOS) of different elements in HEANs.

can be seen in Supporting Information (*SI Appendix*, Fig. S9 and Table S2). The Bader charge analysis shows that there have charge transfer between different elements in HEANs. For example, the charge would accumulate on Pt with a range of 0.37 to 0.69 $|e|$, while other elements are almost positively charged, leading to the potential for adsorption of proton (Fig. 3H). Moreover, the D-band center of the surface atom was calculated as shown in Fig. 3I. Large spin polarization could be found in Fe, Co, and Ni elements, which will be beneficial to the adsorption of O_2 . The wide distribution of D-band centers in HEANs makes it possible to provide diverse active sites for the intermediates during different reactions (11). Specifically, the spin polarization of the active sites will enhance the binding strength of O_2 (*SI Appendix*, Fig. S10 and Table S4). The theoretical calculations and XANES both demonstrate that the high entropy effect leads to the rearrangement of electrons,

which changes the localization degree of electrons, leading to a fine-tuned electronic structure (10, 35).

Electrochemical Performances. To investigate the influence of the defect structure and electronic configuration of HEANs on various electrocatalysis, the commercial catalysts were used as the benchmark, and the materials synthesized by different methods and conditions were compared to further explore the catalytic advantages of HEAN/CNT. First, the catalytic activity of the ORR was studied by linear scanning voltammetry (LSV) at 1,600 rpm with a rotating disk electrode (RDE). Compared with commercial 20% Pt/C and other samples, HEAN/CNT prepared by the high-current shock method exhibits good limiting current density and excellent stability (Fig. 4A). Compared with the infrared fast-heating furnace sample IFHEAN/CNT

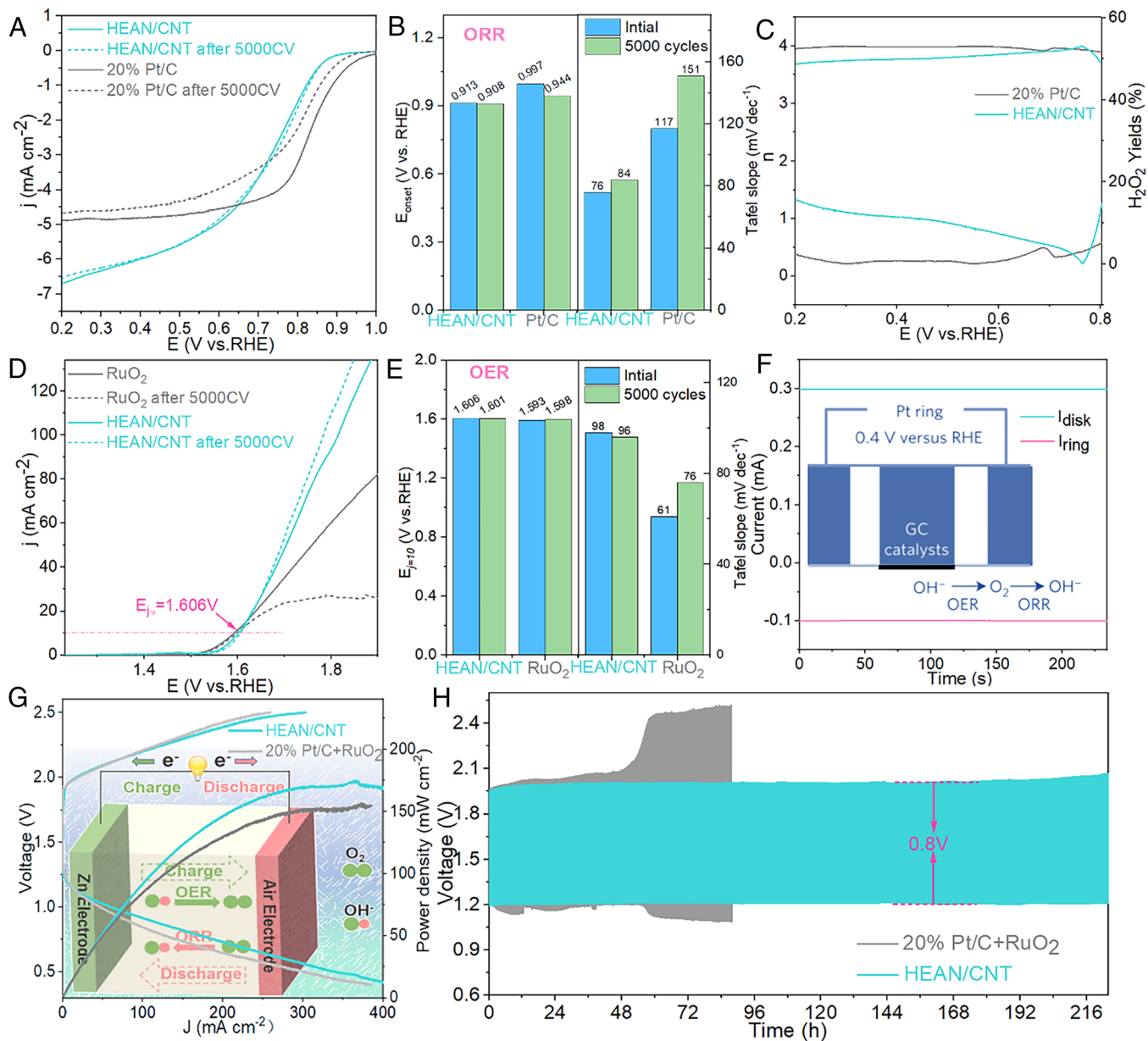


Fig. 4. ORR polarization (A) LSV curves, (B) Tafel plots, and onset potential and (C) electron transfer number (n) and HO_2^- yield at 1,600 rpm for HEAN/CNT and 20%Pt/C. OER polarization (D) LSV curves, (E) Tafel plots and $E_{j=10}$ for HEAN/CNT and RuO₂. (F) Faraday efficiency testing of HEAN/CNT using the RRDE technique in N₂-saturated 1 M KOH solution. The *Inset* presents the Faraday efficiency testing mechanism of the RRDE. (G) Polarization curves and power density of the liquid Zn-air battery and (H) discharge-charge cycling curves of the liquid Zn-air battery for HEAN/CNT and 20%Pt/C+ RuO₂.

(SI Appendix, Fig. S11A), the HEAN/CNT also showed the best performance, indicating that the HEM prepared by the high current impingement method is more homogeneous and the nanoparticles are smaller. Moreover, the ORR properties of Pt/CNT (SI Appendix, Fig. S11B) were not better than those of HEAN/CNT, which indicated that the mixture of various elements gave the material more excellent properties. Fig. 4B compares the changes in the onset potential and the Tafel slope before and after the cycle of the commercial 20% Pt/C catalyst. It can be seen that the HEAN/CNT has no significant difference and a smaller Tafel slope before and after the recycling; at the same time, there is no significant change in the initial potential. However, there is a large difference between the onset potential and the Tafel slope before and after the 20% Pt/C cycle, which further illustrates the excellent stability of HEAN/CNT. The test results of the transfer electron number also show the hydrogen peroxide resistance of HEAN/CNT, indicating the strong stability of the material.

Fig. 4D shows the OER performance of each catalyst tested by RDE at 1,600 rpm. It can be seen from Fig. 4E that the overpotential of HEAN/CNT is close to RuO₂, and the stability is better than RuO₂. The excellent stability of HEAN/CNT is also illustrated by the fact that there is no significant change in the Tafel slope before and after the cycle. In addition, HEAN/CNT exhibited the best OER performance compared with other samples (SI Appendix, Fig. S11 C and D). Fig. 4F shows the Faraday efficiency of HEAN/CNT, and the Faraday efficiency is calculated to be 90% based on the data (36, 37). To confirm the excellent ORR/OER performance of HEAN/CNT, the zinc-air battery test was carried out. Fig. 4G shows the polarization curve of the test of HEAN/CNT and commercial catalyst assembled into the zinc-air battery, according to the battery capacity calculated by the polarization curve, it can be seen that HEAN/CNT and commercial catalyst have similar voltage windows, and HEAN/CNT has a higher energy density than commercial catalysts. As shown in

Fig. 4H, during the long-term cycle stability test of zinc–air batteries, HEAN/CNT still maintains a voltage window of 0.8 V in the cycle of 220 h, however, the voltage window of the commercial catalyst gradually becomes larger after 50 h (38). The test results of the zinc–air battery further confirmed the good stability of HEAN/CNT in the bifunctional catalysis of ORR/OER.

Fig. 5A shows that the catalytic activity of HER of each catalyst was studied by RDE at 1,600 rpm using LSV. It can be seen that the overpotential of HEAN/CNT is not much different from 20% Pt/C, but the cycle stability is much better than Pt/C. Compared with IFHEAN/CNT and Pt/CNT, HEAN/CNT shows good HER performance in *SI Appendix, Fig. S11 E and F*, which further demonstrates the excellent trifunctionality of the HEANs obtained by this method. The overpotential for a current density of -10 mA cm^{-2} and Tafel slope before and after the HEAN/CNT and 20% Pt/C cycles are compared in Fig. 5B. There is not much change in both the overpotential and the Tafel slope before and after the HEAN/CNT cycle, however, the 20% Pt/C increased obviously after the cycle, indicating the stability of HEAN/CNT in HER.

The dual functional characteristics of OER and HER were tested by fully hydrolyzed water. Fig. 5C shows the LSV curve of fully hydrolyzed water, which shows that HEAN/CNT has good and stable electrolyzed water performance compared with commercial catalysts. In the stability test of fully hydrolyzed in Fig. 5D, it can be seen that HEAN/CNT has no attenuation during the electrolyzed water process for more than 20 h, but the commercial catalyst data fluctuates widely and the retention rate is 70% after 19.8 h (39). To detect that the OER and HER processes are indeed oxygen and hydrogen production processes, the generated gas products were detected by an in situ differential electrochemical mass spectrometry (DEMS). From Fig. 5E and F, the corresponding product formation of O_2 and H_2 was detected in the CV cycle interval of OER and HER. As can be seen, the variation trend of O_2 and H_2 yields was consistent with the change of current density, therefore, the DEMS method can prove the occurrence of OER and HER in situ. In addition, the excellent electrochemical performance can be seen from the results of the electrochemical impedance spectroscopy test. It can be seen from *SI Appendix, Fig. S11I* that the

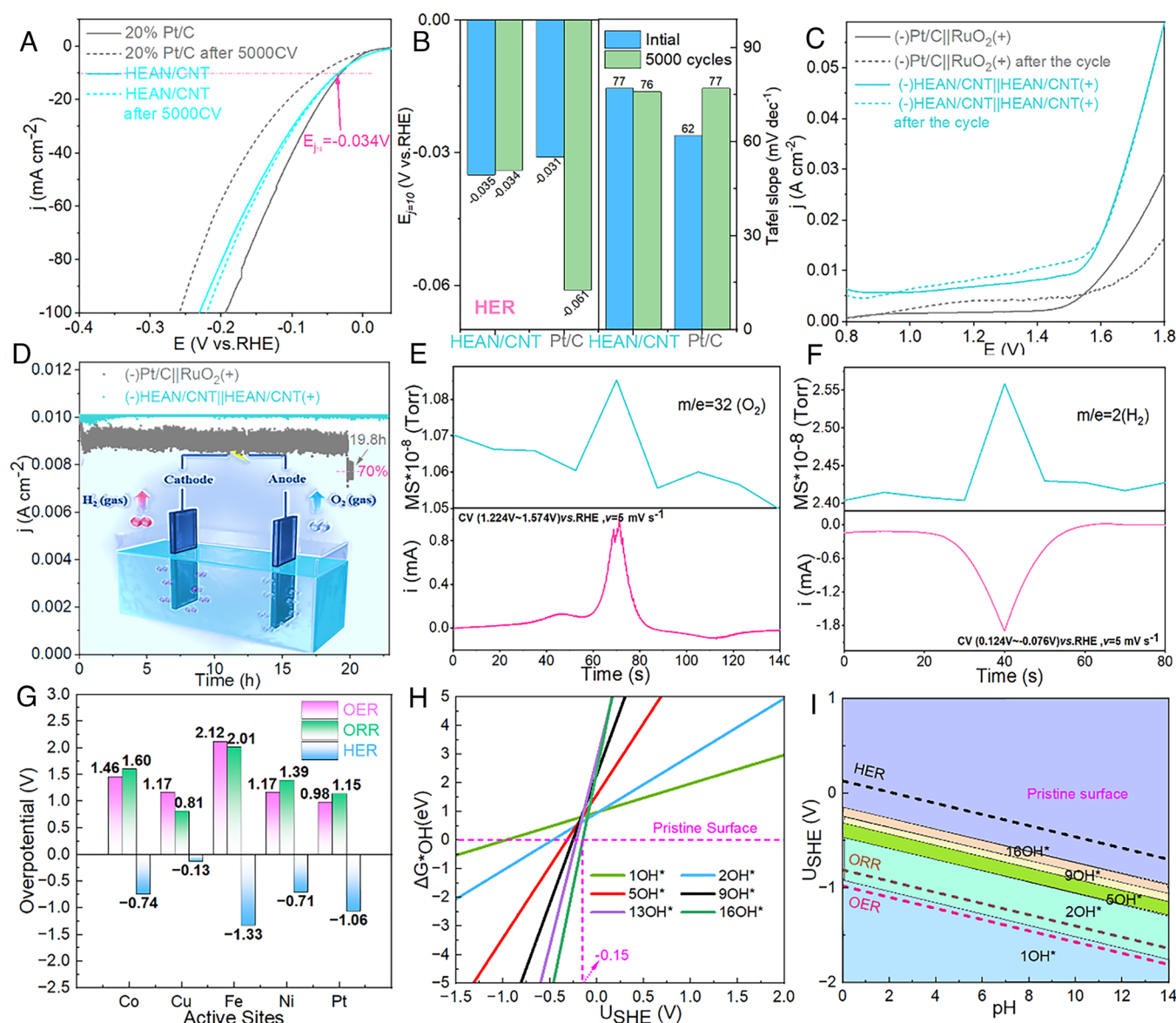


Fig. 5. HER polarization (A) LSV curves, (B) Tafel plots, and $E_{j=10}$ for HEAN/CNT and 20%Pt/C. (C) Polarization curves for overall water splitting and (D) water splitting stability test for HEAN/CNT and (-) 20%Pt/C | RuO₂ (+). (E and F) In situ DEMS for OER and HER. (G) Overpotentials of the OER, ORR, and HER on the active sites of optimal HEANs in a vacuum environment. (H) Surface Pourbaix diagrams of HEANs at pH = 0, and (I) surface Pourbaix diagrams in a wide pH range of HEANs.

prepared HEAN/CNT has a minimum charge transfer resistance, which speeds up the slow chemical kinetics step. Furthermore, the above results show that the electrochemical properties and lifetime of the electrocatalysts can be significantly improved by constructing the defect structure and regulating the electronic arrangement among the multi-elements in HEAN/CNT.

The experimentally shown trifunctionality was further identified by theoretical calculations. Specifically, the fastest OER mainly corresponds to Pt sites with the lowest overpotential of 0.98 V, while ORR active sites correspond to the Cu site with the overpotential of 0.81 V. Meanwhile, the Cu site is also the active sites for HER, due to the closed overpotential to the equilibrium level (Fig. 5G). Besides, the OH⁻ species was observed to cover the surface of HEANs in experiments. Thus, the effects of OH⁻ coverage during the trifunctional processes were considered (Fig. 5H). The calculated Pourbaix diagram indicated that a certain coverage of OH⁻ could facilitate the reaction to a relatively low onset potential, which could be attributed to the OH⁻-induced modulation of local charge states and hydrogen bonding (Fig. 5I).

Mechanism of Multifunctional Electrocatalysis. The electrocatalytic reaction occurs at the interface between solid electrocatalysts and electrolytes, important electrocatalytic reactions involve multi-step

electron and proton transfer processes and may have multiple reaction intermediates. To analyze the mechanism of the trifunctional properties of materials, in situ Raman and FTIR spectroscopy were used to detect signals at different potentials. Moreover, the adjustability of active sites under different reaction conditions was determined by theoretical calculation.

Fig. 6 A–C are the Raman signal of HEAN/CNT in ORR, OER, and HER, respectively. It can be seen that the G peak of the MWCNTs is broadened to a low wavenumber under the potential interval of HER and ORR, this is due to the MWCNTs from semiconducting to metallic properties in the catalytic role of electric conduction (40–42). Similar phenomena were not found in the OER test. It may be that the high potential and rapid oxygen production in the OER test affected the signal. A Raman peak between about 1,610 to 1,620 cm⁻¹ is attributed to the H–O–H bend of water molecules adsorbed on the catalyst surface (43). Compared with the OER process, the peak of HER and ORR shifted to the lower wavenumber, which indicated that the bond of the H₂O molecule was elongated in the active state of the reaction, it is shown that water molecules participate in the process of HER and ORR as reactants under alkaline conditions. There was an obvious peak (1,145 cm⁻¹) at the ORR potential range, and the peak returned to the surface of the material after oxygen

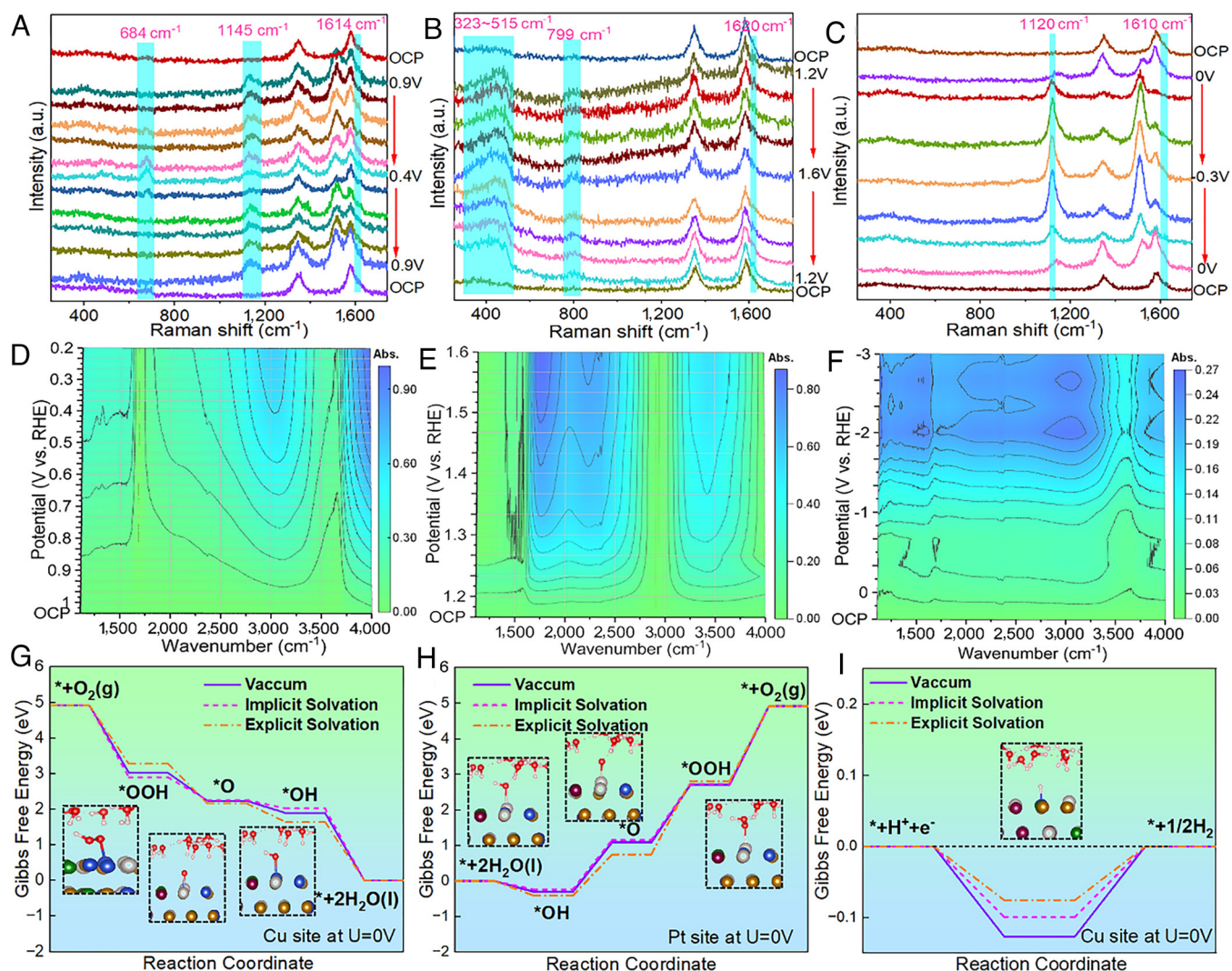


Fig. 6. (A–C) In situ Raman spectra, (D–F) in situ FTIR 2D contour image, and (G–I) Gibbs free energy profiles on different active sites of HEAN/CNT for the ORR, OER, and HER under different solvents.

adsorption. At 684 cm^{-1} , there was an obvious peak at high current density, the peaks here are classified as $^*\text{OOH}$ intermediates. In the OER range, a large bulging peak (323 to 515 cm^{-1}) appeared, indicating that the material was oxidized to oxide or hydroxide at a high potential before OER (44). An obvious peak was observed at 799 cm^{-1} , which belongs to $^*\text{OOH}$. The shift of the $^*\text{OOH}$ absorption peak to a larger wavenumber compared to that in the ORR reaction indicates that the interaction strength of the material with $^*\text{OOH}$ is stronger in the OER process, which indicates that the rate-determining steps of the ORR and OER reactions are different. At $1,120\text{ cm}^{-1}$ of HER potential range, the cyclic variation of the peak with the decrease of the potential, and the decrease of the peak with the increase of the potential was observed, and the peak position shifted to the lower wavenumber with the decrease of the potential. The change here should be attributed to the weak bonding of O and O, and probably the hydrogen release in an alkaline environment is the dissociation of water into hydrated protons in solution, and then the reaction of hydrated protons with water, when the two collide with each other, to form a weak bond between O and O at the lowest energy, $^*\text{H}$ is transferred to the surface of the material in the process, and eventually, the bond becomes hydrogen (45).

Fig. 6 D–F shows the 2D contour image of the FTIR signal of HEAN/CNT in ORR, OER, and HER, respectively. From the results, it can be seen that the peak ($3,030\text{ cm}^{-1}$) appears at the ORR, as the voltage decreases, the peak becomes stronger and shifts to a low wavenumber. In addition, a small peak appeared at $1,280\text{ cm}^{-1}$, which was $^*\text{OOH}$ (46, 47). For the OER interval, significant enhancement peaks were observed at $1,740\text{ cm}^{-1}$ and $3,460\text{ cm}^{-1}$, which were attributed to H_2O from the generation of the surface. The enhancement of the $^*\text{OOH}$ peak was also observed at around $1,250\text{ cm}^{-1}$, the bulge peak at $1,483\text{ cm}^{-1}$ belongs to the bond formed by metal and OOH (48, 49). Moreover, the XPS for OER-catalyzed HEAN/CNT (SI Appendix, Fig. S14) showed that the oxidation state content of various metal elements is increased. The surface reconstruction of HEANs in OER is further explained by the above results. The peak changes of ORR and OER further illustrate the opposite processes of the two reactions (50). In the HER range, the O–H peak at $3,200\text{ cm}^{-1}$ gradually increases and shifts to the lower wavenumber indicating that water consumed in HER changed into hydroxyl radical. The bulge peak that appeared at $2,036\text{ cm}^{-1}$ is of metal hydrogen bonding (51). At $1,286\text{ cm}^{-1}$, an obvious peak was also captured, which corresponded to the signal captured in Raman and further explained that the HER process in an alkaline environment was a weak bonding peak of dissociation of water and then a collision with water. Furthermore, the reaction Gibbs free energies for trifunctional catalyst were further evaluated via DFT calculations by considering both implicit and explicit solvation effects (Fig. 6 G–I and SI Appendix, Fig. S15). The Pt and Cu sites were screened out as the active sites through previous calculations in vacuum conditions (Fig. 5 G). The results indicate that the solvation would influence the binding energies of the reaction intermediates compared to the vacuum (Fig. 6 G). For example, the limiting step of OER on the Pt site was $^*\text{OOH} \rightarrow ^*\text{O}_2$, with the overpotentials of 0.98, 0.96, and 0.88 V for vacuum, implicit and explicit solvation, respectively. Thus, the solvation effects should be taken into consideration for more accurate calculations (52, 53).

Conclusion

In summary, the defect structure and electron interactions for HEANs in this work result in good trifunctional electrocatalysis on ORR, OER, and HER showing good properties and stability

on both zinc–air batteries and fully hydrolyzed water. Moreover, HEAN/CNT has a surface-enhanced effect, and the different signals of the materials in different electrocatalytic reaction regions can be observed by in situ Raman and FTIR. Meanwhile, the DFT results also confirm the electron interaction and the adaptive regulation of active sites in trifunctional catalysis leading to the excellent properties of HEANs. This work thoroughly demonstrates the advantages of HEANs, including their single solid solution phase, tunable active sites, and excellent cycle stability, along with their trifunctional capabilities. The findings affirm that the high-entropy approach is effective in lowering manufacturing costs while maintaining efficient multifunctional electrocatalytic performance.

Materials and Methods

Additional details regarding the materials and methods may be found in SI Appendix.

Acid Treatment of MWCNTs. Add 2 g MWCNTs to 10 mL concentrated nitric acid (HNO_3) and 30 mL concentrated sulfuric acid (H_2SO_4) mixed solution, stir for 2 h at room temperature, and then slowly add deionized water dropwise to a total volume of 120 mL while stirring, resulting mixture is filter washed with 5% hydrochloric acid (HCl), then filtered, and washed with deionized water, and finally filtered and washed with ethanol. The washed MWCNTs are freeze-dried, and the obtained product is marked as ACNT. The freeze-dried ACNT was dispersed into an ethanol solution at a calibrated concentration of 4 mg mL^{-1} for use.

Preparation of Different Catalysts. According to the amount of 20% of the total mass of the metal, five salts of equal atomic ratio of FeCl_3 , NiCl_2 , CoCl_2 , CuCl_2 , and PtCl_2 were added and mixed uniformly with 4 mg mL^{-1} ACNT ultrasound for 2 h, and then freeze-dried to obtain ACNT mixed with five salts, named 5SACNT.

The material that binds 5SACNT tiled between carbon paper and gives carbon paper current impact using In-situ High-tech (CIS-JH3.2.1) to obtain MWCNTs loaded HEANs is named HEAN/CNT.

The contrast materials of a single metal element with 20% metal mass were named Pt/CNT, Fe/CNT, Ni/CNT, Co/CNT, and Cu/CNT, respectively.

The platinum-free material was prepared according to the same method and named NPHEAN/CNT.

HEANs prepared by an infrared rapid-heating furnace named IFHEAN/CNT are obtained by placing 5SACNT in an infrared fast-heating furnace with the fastest heating rate of 50 K s^{-1} to $1,073\text{ K}$.

In Situ Tests. In situ Raman spectra were collected with a 533 nm laser excitation source in O_2 -saturated 0.1 M KOH for ORR and N_2 -saturated 1 M KOH for OER and HER at room temperature. The spectra were collected during the chronoamperometric i-t test at each potential.

In situ infrared external reflection mode IRRAS experiments were collected with 4 cm^{-1} resolution using an FTIR spectrometer (Thermo NICOLET iS50) through a top-plate cell reflection IR setup with a CaF_2 crystal as the infrared transmission window (cutoff energy of $\sim 1,111\text{ cm}^{-1}$) equipped with a liquid nitrogen-cooled MCT detector. Before each measurement of the system, the background spectrum of the catalyst electrode was obtained under the open circuit voltage and the measurement potential of each with an interval of 0.005 V s^{-1} .

In situ differential electrochemical mass spectrometry (DEMS, Hiden Analytical, HPR-40) was collected in the N_2 -saturated 1 M KOH for OER and HER at room temperature.

In addition, the Pt wire was used as the counter electrode and Ag/AgCl was used as the reference electrode for all the in situ experiments.

Data, Materials, and Software Availability. All study data are included in the article and/or SI Appendix.

ACKNOWLEDGMENTS. We would like to acknowledge the financial support provided by the Key National Natural Science Foundation of Yunnan Province (No. 202301AS070040), the Major Science and Technology Projects of Yunnan Province (202302AB080019-3), the National Natural Science Foundation of China (No. 52064049), the Key Laboratory of Solid State Ions for Green Energy

of Yunnan University (2019), the Yunnan University's Research Innovation Fund for Graduate Students (KC-23233757), and the Electron Microscope Center of Yunnan University. Computational resources were provided by the Advanced Computing Center of Yunnan University.

1. Z. W. Seh *et al.*, Combining theory and experiment in electrocatalysis: Insights into materials design. *Science* **355**, eaad4998 (2017).
2. S. Praveen, H. S. Kim, High-entropy alloys: Potential candidates for high-temperature applications—An overview. *Adv. Eng. Mater.* **20**, 1700645 (2018).
3. A. A. H. Tajuddin *et al.*, Corrosion-resistant and high-entropic non-noble-metal electrodes for oxygen evolution in acidic media. *Adv. Mater.* **35**, e2207466 (2023).
4. C. X. Zhao *et al.*, A $\Delta E = 0.63$ V bifunctional oxygen electrocatalyst enables high-rate and long-cycling zinc-air batteries. *Adv. Mater.* **33**, e2008606 (2021).
5. L. Zhang, W. Cai, N. Bao, H. Yang, Implanting an electron donor to enlarge the d-p hybridization of high-entropy (Oxy)hydroxide: A novel design to boost oxygen evolution. *Adv. Mater.* **34**, e2110511 (2022).
6. Y. Sun *et al.*, A general approach to high-entropy metallic nanowire electrocatalysts. *Matter* **6**, 193–205 (2023).
7. R. Li *et al.*, Design of hierarchical porosity via manipulating chemical and microstructural complexities in high-entropy alloys for efficient water electrolysis. *Adv. Sci.* **9**, e2105808 (2022).
8. Y. G. Yao *et al.*, Extreme mixing in nanoscale transition metal alloys. *Matter* **4**, 2340–2353 (2021).
9. Y. Ma *et al.*, High-entropy energy materials: Challenges and new opportunities. *Energy Environ. Sci.* **14**, 2883–2905 (2021).
10. H. D. Li, J. P. Lai, Z. J. Li, L. Wang, Multi-sites electrocatalysis in high-entropy alloys. *Adv. Funct. Mater.* **31**, 2106715 (2021).
11. L. Tao *et al.*, A general synthetic method for high-entropy alloy subnanometer ribbons. *J. Am. Chem. Soc.* **144**, 10582–10590 (2022).
12. H. Zhu *et al.*, A high-entropy atomic environment converts inactive to active sites for electrocatalysis. *Energy Environ. Sci.* **16**, 619–628 (2023).
13. Y. Yao *et al.*, Carbothermal shock synthesis of high-entropy-alloy nanoparticles. *Science* **359**, 1489–1494 (2018).
14. F. Chen *et al.*, High-temperature atomic mixing toward well-dispersed bimetallic electrocatalysts. *Adv. Energy Mater.* **8**, 1800466 (2018).
15. W. Shi *et al.*, Transient and general synthesis of high-density and ultrasmall nanoparticles on two-dimensional porous carbon via coordinated carbothermal shock. *Nat. Commun.* **14**, 2294 (2023).
16. C. Li *et al.*, Ultrafast self-heating synthesis of robust heterogeneous nanocarbides for high current density hydrogen evolution reaction. *Nat. Commun.* **13**, 3338 (2022).
17. T. Y. Li *et al.*, Carbon-supported high-entropy oxide nanoparticles as stable electrocatalysts for oxygen reduction reactions. *Adv. Funct. Mater.* **31**, 2010561 (2021).
18. J. Hao *et al.*, Unraveling the electronegativity-dominated intermediate adsorption on high-entropy alloy electrocatalysts. *Nat. Commun.* **13**, 2662 (2022).
19. D. Wu *et al.*, Noble-metal high-entropy-alloy nanoparticles: Atomic-level insight into the electronic structure. *J. Am. Chem. Soc.* **144**, 3365–3369 (2022).
20. Y. Li *et al.*, High-entropy-alloy nanoparticles with enhanced interband transitions for efficient photothermal conversion. *Angew. Chem. Int. Ed. Engl.* **60**, 27113–27118 (2021).
21. W. R. Zhang, P. K. Liaw, Y. Zhang, Science and technology in high-entropy alloys. *Sci. China Mater.* **61**, 2–22 (2018).
22. Y. Yao *et al.*, High-entropy nanoparticles: Synthesis-structure-property relationships and data-driven discovery. *Science* **376**, eabn3103 (2022).
23. Y. Lin *et al.*, Analytical transmission electron microscopy for emerging advanced materials. *Matter* **4**, 2309–2339 (2021).
24. M. J. Hytch, E. Snoeck, R. Kilaas, Quantitative measurement of displacement and strain fields from HREM micrographs. *Ultramicroscopy* **74**, 131–146 (1998).
25. Z. Huang *et al.*, Direct observation of the formation and stabilization of metallic nanoparticles on carbon supports. *Nat. Commun.* **11**, 6373 (2020).
26. D. Watanabe, P. M. J. Fisher, Electron diffraction study of order in the CuAu₃ alloys. *J. Phys. Soc. Japan* **20**, 2170–2179 (1965).
27. R. de Ridder, G. van Tendeloo, S. Amelinckx, Electron microscopic study of the chimney ladder structures MnSi₂–x and MoGe₂–x. *Phys. Status Solidi A* **33**, 383–393 (1976).
28. G. van Tendeloo, R. de Ridder, D. van Dyck, J. van Landuyt, S. Amelinckx, Microstructural study of copper-intercalated niobium disulphide and tantalum disulphide Cu_xNbS₂ and Cu_xTaS₂. Order-disorder transitions and incommensurate superstructures in Cu_xNbS₂ (0.8 < x < 1). *Phys. Status Solidi A* **38**, 185–198 (1976).
29. W. Bian *et al.*, Direct identification of surface defects and their influence on the optical characteristics of upconversion nanoparticles. *ACS Nano* **12**, 3623–3628 (2018).
30. X. Liu *et al.*, Tunable cationic vacancies of cobalt oxides for efficient electrocatalysis in Li–O₂ batteries. *Adv. Energy Mater.* **10**, 2001415 (2020).
31. X. Zhao, S. Sun, F. Yang, Y. Li, Atomic-scale evidence of catalyst evolution for the structure-controlled growth of single-walled carbon nanotubes. *Acc. Chem. Res.* **55**, 3334–3344 (2022).
32. Z. W. Yin *et al.*, Advanced electron energy loss spectroscopy for battery studies. *Adv. Funct. Mater.* **32**, 2107190 (2021).
33. G. Feng *et al.*, Sub-2 nm ultrasmall high-entropy alloy nanoparticles for extremely superior electrocatalytic hydrogen evolution. *J. Am. Chem. Soc.* **143**, 17117–17127 (2021).
34. P. Rao *et al.*, Movable type printing method to synthesize high-entropy single-atom catalysts. *Nat. Commun.* **13**, 5071 (2022).
35. J. Kwon *et al.*, Tailored electronic structure of Ir in high entropy alloy for highly active and durable bifunctional electrocatalyst for water splitting under an acidic environment. *Adv. Mater.* **35**, e2300091 (2023).
36. S. Zhao *et al.*, Ultrathin metal-organic framework nanosheets for electrocatalytic oxygen evolution. *Nat. Energy* **1**, 16184 (2016).
37. J. Suntivich, K. J. May, H. A. Gasteiger, J. B. Goodenough, Y. Shao-Horn, A perovskite oxide optimized for oxygen evolution catalysis from molecular orbital principles. *Science* **334**, 1383–1385 (2011).
38. J. Diao *et al.*, Interfacial engineering of W₂N/WC heterostructures derived from solid-state synthesis: A highly efficient trifunctional electrocatalyst for ORR, OER, and HER. *Adv. Mater.* **32**, e1905679 (2020).
39. H. Liu *et al.*, Metal-organic-framework-derived Co₃P nanoparticle/multi-doped porous carbon as a trifunctional electrocatalyst. *Adv. Mater.* **32**, e2003649 (2020).
40. S. D. M. Brown *et al.*, Origin of the Breit-Wigner-Fano lineshape of the tangential G-band feature of metallic carbon nanotubes. *Phys. Rev. B* **63**, 155414 (2001).
41. M. A. Pimenta *et al.*, Raman modes of metallic carbon nanotubes. *Phys. Rev. B* **58**, R16016–R16019 (1998).
42. A. Jorio, R. Saito, G. Dresselhaus, M. S. Dresselhaus, "The G-band and time-independent perturbations" in *Raman Spectroscopy in Graphene Related Systems* (WILEY-VCH Verlag GmbH & Co. KGaA, 2011), pp. 159–177, 10.1002/9783527632695.ch7.
43. L. F. Shen *et al.*, Interfacial structure of water as a new descriptor of the hydrogen evolution reaction. *Angew. Chem. Int. Ed. Engl.* **59**, 22397–22402 (2020).
44. Y. Deng, B. S. Yeo, Characterization of electrocatalytic water splitting and CO₂ reduction reactions using in situ/operando Raman spectroscopy. *ACS Catal.* **7**, 7873–7889 (2017).
45. Y. Tian *et al.*, Visualizing Eigen/Zundel cations and their interconversion in monolayer water on metal surfaces. *Science* **377**, 315–319 (2022).
46. M. Li *et al.*, Proximity electronic effect of Ni/Co diatomic sites for synergistic promotion of electrocatalytic oxygen reduction and hydrogen evolution. *Adv. Funct. Mater.* **33**, 2210867 (2022).
47. X. Wei *et al.*, Tuning the spin state of Fe single atoms by Pd nanoclusters enables robust oxygen reduction with dissociative pathway. *Chem* **9**, 181–197 (2023).
48. X. Sun *et al.*, In situ construction of flexible V–Ni redox centers over Ni-based MOF nanosheet arrays for electrochemical water oxidation. *Small Methods* **5**, e2100573 (2021).
49. Y. Hu *et al.*, Understanding the sulphur-oxygen exchange process of metal sulphides prior to oxygen evolution reaction. *Nat. Commun.* **14**, 1949 (2023).
50. W. Cheng *et al.*, Lattice-strained metal-organic-framework arrays for bifunctional oxygen electrocatalysis. *Nat. Energy* **4**, 115–122 (2019).
51. Q. He *et al.*, Synergic reaction kinetics over adjacent ruthenium sites for superb hydrogen generation in alkaline media. *Adv. Mater.* **34**, e2110604 (2022).
52. H. B. Tao *et al.*, A general method to probe oxygen evolution intermediates at operating conditions. *Joule* **3**, 1498–1509 (2019).
53. Y. Cao *et al.*, Surface hydroxide promotes CO₂ electrolysis to ethylene in acidic conditions. *Nat. Commun.* **14**, 2387 (2023).

Author affiliations: ^aSchool of Materials and Energy, International Joint Research Center for Advanced Energy Materials of Yunnan Province, Yunnan Key Laboratory of Carbon Neutrality and Green Low-carbon Technologies, Yunnan University, Kunming 650091, China; ^bDepartment of Physics and Electronic Engineering, Yancheng Teachers University, Yancheng 224002, China; and ^cSouthwest United Graduate School, Kunming 650091, China